Research Article | Vol. 26, No. 20 | 1 Oct 2018 | OPTICS EXPRESS 25582
Optics EXPRESS

Adiabatic four-wave mixing frequency conversion

EYAL BAHAR,[1,3] XIAOYUE DING,[2,3] ASAF DAHAN,[1] HAIM SUCHOWSKI,[1] AND JEFFREY MOSES[2,*]

[1]*Raymond and Beverly Sackler School of Physics and Astronomy, Tel Aviv University, Tel Aviv 69978, Israel*
[2]*School of Applied and Engineering Physics, Cornell University, Ithaca, NY 14853, USA*
[3]*These authors contributed equally to this work*
[*]*moses@cornell.edu*

Abstract: We introduce the concept of adiabatic four-wave mixing (AFMW) frequency conversion in cubic nonlinear media through an analogy to dynamics in quantum two-level systems. Rapid adiabatic passage in four-wave mixing enables coherent near-100% photon number down-conversion or up-conversion over a bandwidth much larger than ordinary phase-matching bandwidths, overcoming the normal efficiency-bandwidth trade-off. We develop numerical methods to simulate AFWM pulse propagation in silicon photonics and fiber platforms as examples. First, we show that with a longitudinally varying silicon waveguide structure, a bandwidth of 70 nm centered at 1820 nm can be generated with 90% photon number conversion. Second, we predict the broadband generation of nanojoule energy, 4.2-5.2 μm mid-infrared light in a short, linearly tapered fluoride step-index fiber. We expect the AFWM concept to be broadly applicable to cubic nonlinear platforms, for applications as diverse as bright ultrafast light pulse generation, sensing, and conversion between telecommunications bands.

OCIS codes: (320.0320) Ultrafast optics; (190.0190) Nonlinear optics; (190.4380) Nonlinear optics, four-wave mixing.

References and links

1. M. A. Foster, A. C. Turner, R. Salem, M. Lipson, and A. L. Gaeta, "Broad-band continuous-wave parametric wavelength conversion in silicon nanowaveguides," Opt. Express **15**, 12949–12958 (2007).
2. J. Leuthold, C. Koos, and W. Freude, "Nonlinear silicon photonics," Nat. Photonics **4**, 535–544 (2010).
3. M. G. Allen, "Diode laser absorption sensors for gas-dynamic and combustion flows," Meas. Sci. Technol. **9**, 545–562 (1998).
4. J. Wang, J. Sun, and Q. Sun, "Proposal for all-optical switchable or/xor logic gates using sum-frequency generation," IEEE Photonics Technol. Lett. **19**, 541–543 (2007).
5. D. Polli, P. Altoè, O. Weingart, K. M. Spillane, C. Manzoni, D. Brida, G. Tomasello, G. Orlandi, P. Kukura, R. A. Mathies, M. Garavelli, and G. Cerullo, "Conical intersection dynamics of the primary photoisomerization event in vision," Nature. **467**, 440–443 (2010).
6. T. Popmintchev, M.-C. Chen, D. Popmintchev, P. Arpin, S. Brown, S. Ališauskas, G. Andriukaitis, T. Balčiunas, O. D. Mücke, A. Pugzlys, A. Baltuška, B. Shim, S. E. Schrauth, A. Gaeta, C. Hernández-García, L. Plaja, A. Becker, A. Jaron-Becker, M. M. Murnane, and H. C. Kapteyn, "Bright coherent ultrahigh harmonics in the kev x-ray regime from mid-infrared femtosecond lasers," Science. **336**, 1287–1291 (2012).
7. H. Suchowski, D. Oron, A. Arie, and Y. Silberberg, "Geometrical representation of sum frequency generation and adiabatic frequency conversion," Phys. Rev. A **78**, 063821 (2008).
8. H. Suchowski, V. Prabhudesai, D. Oron, A. Arie, and Y. Silberberg, "Robust adiabatic sum frequency conversion," Opt. Express **17**, 12731–12740 (2009).
9. H. Suchowski, B. D. Bruner, A. Ganany-Padowicz, I. Juwiler, A. Arie, and Y. Silberberg, "Adiabatic frequency conversion of ultrafast pulses," Appl. Phys. B **105**, 697–702 (2011).
10. J. Moses, H. Suchowski, and F. X. Kärtner, "Fully efficient adiabatic frequency conversion of broadband ti: sapphire oscillator pulses," Opt. Lett. **37**, 1589–1591 (2012).
11. H. Suchowski, P. R. Krogen, S.-W. Huang, F. X. Kärtner, and J. Moses, "Octave-spanning coherent mid-ir generation via adiabatic difference frequency conversion," Opt. Express **21**, 28892–28901 (2013).
12. P. Krogen, H. Suchowski, H. Liang, N. Flemens, K.-H. Hong, F. X. Kärtner, and J. Moses, "Generation and multi-octave shaping of mid-infrared intense single-cycle pulses," Nat. Photonics **11**, 222–226 (2017).
13. M. Charbonneau-Lefort, B. Afeyan, and M. M. Fejer, "Optical parametric amplifiers using chirped quasi-phase-matching gratings i: practical design formulas," J. Opt. Soc. Am. B **25**, 463–480 (2008).

#337901 https://doi.org/10.1364/OE.26.025582
Journal © 2018 Received 11 Jul 2018; revised 29 Aug 2018; accepted 30 Aug 2018; published 17 Sep 2018

Optics EXPRESS

14. C. Phillips and M. Fejer, "Efficiency and phase of optical parametric amplification in chirped quasi-phase-matched gratings," Opt. Lett. **35**, 3093–3095 (2010).
15. C. Phillips and M. Fejer, "Adiabatic optical parametric oscillators: steady-state and dynamical behavior," Opt. Express **20**, 2466–2482 (2012).
16. C. Heese, C. R. Phillips, B. W. Mayer, L. Gallmann, M. M. Fejer, and U. Keller, "75 mw few-cycle mid-infrared pulses from a collinear apodized appln-based opcpa," Opt. Express **20**, 26888–26894 (2012).
17. O. Yaakobi, L. Caspani, M. Clerici, F. Vidal, and R. Morandotti, "Complete energy conversion by autoresonant three-wave mixing in nonuniform media," Opt. Express **21**, 1623–1632 (2013).
18. A. Markov, A. Mazhorova, H. Breitenborn, A. Bruhacs, M. Clerici, D. Modotto, O. Jedrkiewicz, P. di Trapani, A. Major, F. Vidal, and R. Morandotti, "Broadband and efficient adiabatic three-wave-mixing in a temperature-controlled bulk crystal," Opt. Express **26**, 4448–4458 (2018).
19. M. A. Foster, A. C. Turner, J. E. Sharping, B. S. Schmidt, M. Lipson, and A. L. Gaeta, "Broad-band optical parametric gain on a silicon photonic chip," Nature **441**, 960–963 (2006).
20. Y. Ding, J. Xu, H. Ou, and C. Peucheret, "Mode-selective wavelength conversion based on four-wave mixing in a multimode silicon waveguide," Opt. Express **22**, 127–135 (2014).
21. I. Agha, M. Davanço, B. Thurston, and K. Srinivasan, "Low-noise chip-based frequency conversion by four-wave-mixing bragg scattering in sinx waveguides," Opt. Lett. **37**, 2997–2999 (2012).
22. S. Coen, A. H. L. Chau, R. Leonhardt, J. D. Harvey, J. C. Knight, W. J. Wadsworth, and P. S. J. Russell, "Supercontinuum generation by stimulated raman scattering and parametric four-wave mixing in photonic crystal fibers," J. Opt. Soc. Am. B **19**, 753–764 (2002).
23. C. R. Petersen, U. Møller, I. Kubat, B. Zhou, S. Dupont, J. Ramsay, T. Benson, S. Sujecki, N. Abdel-Moneim, Z. Tang, D. Furniss, A. Seddon, and O. Bang, "Mid-infrared supercontinuum covering the 1.4–13.3 μm molecular fingerprint region using ultra-high na chalcogenide step-index fibre," Nat. Photonics **8**, 830–834 (2014).
24. K. Yin, B. Zhang, L. Yang, and J. Hou, "15.2 w spectrally flat all-fiber supercontinuum laser source with> 1 w power beyond 3.8 μm," Opt. Lett. **42**, 2334–2337 (2017).
25. C. Y. Wang, T. Herr, P. Del'Haye, A. Schliesser, J. Hofer, R. Holzwarth, T. Hänsch, N. Picqué, and T. J. Kippenberg, "Mid-infrared optical frequency combs at 2.5 μm based on crystalline microresonators," Nat. Commun. **4**, 1345 (2013).
26. P. Del'Haye, O. Arcizet, A. Schliesser, R. Holzwarth, and T. J. Kippenberg, "Full stabilization of a microresonator-based optical frequency comb," Phys. Rev. Lett. **101**, 053903 (2008).
27. A. G. Griffith, R. K. Lau, J. Cardenas, Y. Okawachi, A. Mohanty, R. Fain, Y. H. D. Lee, M. Yu, C. T. Phare, C. B. Poitras, A. L. Gaeta, and M. Lipson, "Silicon-chip mid-infrared frequency comb generation," Nat. Commun. **6**, 6299 (2015).
28. S. B. Papp, K. Beha, P. Del'Haye, F. Quinlan, H. Lee, K. J. Vahala, and S. A. Diddams, "Microresonator frequency comb optical clock," Optica. **1**, 10–14 (2014).
29. M. Nisoli, S. De Silvestri, and O. Svelto, "Generation of high energy 10 fs pulses by a new pulse compression technique," Appl. Phys. Lett. **68**, 2793–2795 (1996).
30. D. Faccio, A. Grün, P. K. Bates, O. Chalus, and J. Biegert, "Optical amplification in the near-infrared in gas-filled hollow-core fibers," Opt. Lett. **34**, 2918–2920 (2009).
31. J. Fatome, S. Pitois, and G. Millot, "20-ghz-to-1-thz repetition rate pulse sources based on multiple four-wave mixing in optical fibers," IEEE J. Quantum Electron. **42**, 1038–1046 (2006).
32. C. McKinstrie, S. Radic, M. Raymer, and L. Schenato, "Unimpaired phase-sensitive amplification by vector four-wave mixing near the zero-dispersion frequency," Opt. Express **15**, 2178–2189 (2007).
33. A. C. S Jr, J. C. Boggio, A. Rieznik, H. Hernandez-Figueroa, H. Fragnito, and J. Knight, "Highly efficient generation of broadband cascaded four-wave mixing products," Opt. Express **16**, 2816–2828 (2008).
34. T. T. Ng, J. L. Blows, J. T. Mok, R. W. McKerracher, and B. J. Eggleton, "Cascaded four-wave mixing in fiber optical parametric amplifiers: application to residual dispersion monitoring," J. Light. Technol. **23**, 818–826 (2005).
35. K. Inoue, "Tunable and selective wavelength conversion using fiber four-wave mixing with two pump lights," IEEE Photonics Technol. Lett. **6**, 1451–1453 (1994).
36. C. McKinstrie, J. Harvey, S. Radic, and M. Raymer, "Translation of quantum states by four-wave mixing in fibers," Opt. Express **13**, 9131–9142 (2005).
37. G. Agrawal, *Nonlinear Fiber Optics* (Academic Press, 2012).
38. B. W. Shore, *The Theory of Coherent Atomic Excitation* (Wiley, 1996).
39. T. Rickes, L. Yatsenko, S. Steuerwald, T. Halfmann, B. Shore, N. Vitanov, and K. Bergmann, "Efficient adiabatic population transfer by two-photon excitation assisted by a laser-induced stark shift," The J. Chem. Phys. **113**, 534–546 (2000).
40. H. Kogelnik, "Theory of dielectric waveguides," in *Integrated Optics,* T. Tamir, ed. (Springer Berlin Heidelberg, 1975), pp. 13–81.
41. R. W. Boyd, *Nonlinear optics* (Academic Press, 2003).
42. A. Levanon, A. Dahan, A. Nagler, E. Lifshitz, E. Bahar, M. Mrejen, and H. Suchowski, "Pulse shaping of broadband adiabatic shg from a ti-sapphire oscillator," Opt. Lett. **42**, 2992–2995 (2017).
43. J. B. Christensen, J. G. Koefoed, B. Bell, C. McKinstrie, and K. Rottwitt, "Shape-preserving and unidirectional frequency conversion by four-wave mixing," Opt. Express **26**, 17145–17157 (2018).

Optics EXPRESS

44. A. C. Turner, C. Manolatou, B. S. Schmidt, M. Lipson, M. A. Foster, J. E. Sharping, and A. L. Gaeta, "Tailored anomalous group-velocity dispersion in silicon channel waveguides," Opt. Express **14**, 4357–4362 (2006).
45. L. Tong, J. Lou, and E. Mazur, "Single-mode guiding properties of subwavelength-diameter silica and silicon wire waveguides," Opt. Express **12**, 1025–1035 (2004).
46. Y. Tang, L. G. Wright, K. Charan, T. Wang, C. Xu, and F. W. Wise, "Generation of intense 100 fs solitons tunable from 2 to 4.3 μm in fluoride fiber," Optica **3**, 948–951 (2016).
47. L. D. Landau, "Zur theorie der energieubertragung ii," Phys. Sov. Union **2**, 46–51 (1932).
48. C. Zener, "Non-adiabatic crossing of energy levels," Proc. Royal S. L. A **137**, 696–702 (1932).
49. A. M. Heidt, Z. Li, J. Sahu, P. C. Shardlow, M. Becker, M. Rothhardt, M. Ibsen, R. Phelan, B. Kelly, S. U. Alam, and D. J. Richardson, "100 kw peak power picosecond thulium-doped fiber amplifier system seeded by a gain-switched diode laser at 2 μm," Opt. Lett. **38**, 1615–1617 (2013).
50. G. Krauss, S. Lohss, T. Hanke, A. Sell, S. Eggert, R. Huber, and A. Leitenstorfer, "Synthesis of a single cycle of light with compact erbium-doped fibre technology," Nat. Photonics **4**, 33–36 (2010).
51. M. S. Habib, C. Markos, O. Bang, and M. Bache, "Soliton-plasma nonlinear dynamics in mid-ir gas-filled hollow-core fibers," Opt. Lett. **42**, 2232–2235 (2017).
52. T. Tanemura, C. S. Goh, K. Kikuchi, and S. Y. Set, "Highly efficient arbitrary wavelength conversion within entire c-band based on nondegenerate fiber four-wave mixing," IEEE Photonics Technol. Lett. **16**, 551–553 (2004).
53. H. McGuinness, M. Raymer, C. McKinstrie, and S. Radic, "Quantum frequency translation of single-photon states in a photonic crystal fiber," Phys. Rev. Lett. **105**, 093604 (2010).
54. Q. Li, M. Davanço, and K. Srinivasan, "Efficient and low-noise single-photon-level frequency conversion interfaces using silicon nanophotonics," Nat. Photonics **10**, 406–414 (2016).
55. S. Clemmen, A. Farsi, S. Ramelow, and A. L. Gaeta, "Ramsey interference with single photons," Phys. Rev. Lett. **117**, 223601 (2016).
56. S. Clemmen, A. Farsi, S. Ramelow, and A. L. Gaeta, "All-optically tunable buffer for single photons," Opt. Lett. **43**, 2138–2141 (2018).
57. C. Joshi, A. Farsi, S. Clemmen, S. Ramelow, and A. L. Gaeta, "Frequency multiplexing for quasi-deterministic heralded single-photon sources," Nat. Commun. **9**, 847 (2018).

1. Introduction

Efficient and robust frequency conversion of broadband optical pulses is essential for fields ranging from pure science to technology industries, including integrated photonics for telecommunications and the next generation of computers [1, 2], environmental detection devices [3], optical signal processing for applications such as encoding and encryption [4], as well as strong field applications such as X-ray generation and multidimensional spectroscopies for understanding the fundamental ultrafast dynamics of molecules [5, 6].

In recent years, much effort has been invested in developing schemes to efficiently convert broader and broader optical spectra. Yet the common paradigm of nonlinear frequency conversion with constant phase matching includes a restrictive trade-off between the conversion efficiency and its bandwidth. Our recent demonstrations of the adiabatic frequency conversion concept in three-wave mixing processes introduced the ability to sidestep the efficiency-bandwidth trade-off in sum-frequency generation (SFG) and difference-frequency generation (DFG) [7–10], dramatically increasing the available bandwidth while also ensuring a high conversion efficiency. Application of this concept in aperiodically poled quasi-phase-matched media allowed the generation of phase- and amplitude-controlled, octave-spanning, coherent mid-IR light sources [11, 12]. Moreover, the amplitude and phase transferability of adiabatic frequency conversion enables arbitrary amplitude and phase tunability by pulse shaping prior to conversion. This allowed the arbitrary shaping of single-cycle pulses and promises great flexibility for ultrafast spectroscopic applications [12]. Broadband optical parametric amplification (OPA) and optical parametric oscillation (OPO) have also been investigated to show greatly enhanced conversion efficiency in aperiodically poled quasi-phase-matched media and nonuniform media [13–18]. Though the adiabatic frequency conversion concept is very promising, the traditional platforms for frequency conversion using three-wave mixing processes are limited to devices based on specialized materials engineered and grown specifically for the application, whether for ultrashort pulses or for single-frequency sources.

In contrast, the ubiquitous presence of cubic optical nonlinearities enables all devices employing

Optics EXPRESS

light propagation the capacity for frequency conversion via four-wave mixing (FWM). Recent examples include optical parametric gain and frequency conversion in silicon waveguides used for telecommunications [1, 19–21], supercontinuum generation in optical fibers made from a wide range of materials and with a diverse set of structures [22–24], dielectric and semiconductor microresonators used for supercontinuum or frequency comb generation [25–28], and gas filled capillaries used for spectral broadening or parametric amplification of ultrashort pulses [29, 30]. In each of these technologies, FWM frequency conversion has been employed. Like all nonlinear frequency conversion methods, applications of FWM to the generation of broadband light sources are limited by a trade-off between efficiency and bandwidth. Furthermore, the commonly used technique for frequency conversion, cascaded FWM [31–34], does not allow flexible control of the spectral phase of the converted light.

Here, we introduce the concept of adiabatic frequency conversion in FWM, which we find broadly applicable to $\chi^{(3)}$ nonlinear platforms. We develop a theoretical framework for rapid adiabatic passage in FWM, analogous to the dynamics of quantum two-level systems. We show that a conversion efficiency asymptotically approaching 100% over broad bandwidth can be achieved if the adiabatic condition is met, overcoming the traditional efficiency-bandwidth trade-off in common FWM frequency conversion processes. As examples, we apply the theory to silicon photonics and step-index fibers, two of the $\chi^{(3)}$ nonlinear platforms most widely used in applications, using generalized pulsed beam propagation simulations. We find near-100% photon conversion efficiency can be achieved by a simple longitudinal tuning of waveguide dimensions, generating broad bandwidths in either near-IR or mid-IR wavelength ranges. We expect FWM frequency conversion in many other platforms and at many other wavelengths would benefit from this process in a similar fashion.

The article is organized as follows. In Section 2, we present the SU(2) symmetry present in FWM frequency conversion under the strong pump approximation, which illuminates the similarity of photon conversion in FWM to population exchange in two-level systems. We then discuss the conditions for achieving rapid adiabatic passage in FWM. Compared to adiabatic evolution in $\chi^{(2)}$ media, several new characteristics are observed. In Section 3, we present generalized propagation equations for FWM derived from Maxwell's equations. We develop numerical methods capturing the full frequency- and time-domain nonlinear pulse propagation effects for waveguided interactions, including exact broadband dispersion, self- and cross-phase modulation, and the FWM process used for adiabatic frequency conversion. We focus on particular features of broadband pulse propagation in waveguided media that may be essential for a given application of adiabatic four wave mixing (AFWM), such as the evaluation of accurate relative strengths of nonlinear effects over a large frequency range as well as the capture of additional parasitic degenerate and non-degenerate FWM processes.

In Section 4, we numerically solve the generalized equations in order to explore silicon photonic devices and optical fiber platforms for realizing AFWM. For silicon photonic devices, we show generation of a 70-nm bandwidth centered at 1820 nm with a photon conversion efficiency greater than 90%. Our solution, which does not require a strong pump condition, is the first solution that allows such wide spectral widths with high conversion efficiency. For step-index fibers, we present the optimal fiber parameters for phase matching AFWM frequency conversion. By modeling a tapered commercially available fluoride step-index fiber, we predict that nanojoule energy, 4.2-5.2 μm broadband mid-IR pulses could be realized by an all-fiber based system, being among the most energetic mid-IR fiber sources in this spectral range. Because the AFWM mechanism is fundamental, we believe our findings will open new routes for achieving energetic and broadband generation over large frequency ranges where other methods suffer from either low spectral power or narrow bandwidth due to the efficiency-bandwidth trade-off, such as frequency conversion in on-chip photonic devices for telecom and innovative computers, as well as fiber-based down-conversion (mid-IR) and up-conversion (UV) sources for high-repetition-rate

Optics EXPRESS

spectroscopy or low-repetition-rate high-intensity applications.

2. Concepts and theory

We begin by introducing the concept of AFWM underlying the new broadband and efficient FWM frequency conversion paradigm. To establish an intuitive physical picture, we make an analogy between FWM frequency conversion and coupled two-level systems through demonstration of SU(2) symmetry present in FWM processes under the strong pump approximation. We then establish the adiabatic condition for achieving AFWM. In the following sections, we will explore the more general nonlinear dynamics of broadband pulsed waves in a waveguided geometry.

2.1. Analogy to population transfer in a two-level system possessing SU(2) symmetry

As in three-wave mixing processes [7], under certain conditions photon transfer in a FWM process can be understood by analogy to population transfer in a two-level quantum atom possessing SU(2) symmetry. These are the conditions under which a fully adiabatic, one-to-one transfer of photons between frequencies becomes possible. Consider FWM in a $\chi^{(3)}$ nonlinear medium by the schemes shown in Fig. 1(a), commonly known as four-wave mixing Bragg scattering (FWM-BS) [35, 36], and Fig. 1(b), with initial photon numbers n_{A}, n_{B}, n_{Sig}, and n_{Idl}, for $\mathrm{Pump_A}$, $\mathrm{Pump_B}$, Signal, and Idler waves, respectively. When satisfying the conditions $n_{\mathrm{A}}, n_{\mathrm{B}} \gg n_{\mathrm{Sig}}, n_{\mathrm{Idl}}$ under either scheme, an exchange of n photons will leave the four waves with approximate photon numbers n_{A}, n_{B}, $n_{\mathrm{Sig}} - n$, and $n_{\mathrm{Idl}} + n$. An exchange of photons between four waves is thus approximately reduced to a one-to-one photon number transfer between the signal and idler waves, resembling population exchange in a two-level system. Experimentally, these conditions can be met if the intensities of the two pumps are assumed to be much stronger than those of the signal and idler waves.

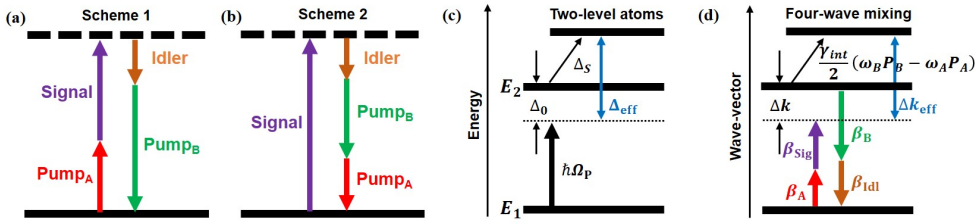

Fig. 1. Energy diagrams of two schemes of four-wave mixing, and the analogy between two-level atoms and FWM. **(a)** Annihilation of *Signal* and *Pump A* photons allows creation of *Idler* and *Pump B* photons. This scheme is known as four-wave mixing Bragg scattering. **(b)** Annihilation of a *Signal* photon allows creation of *Pump A*, *Pump B*, and *Idler* photons. In both cases, when pump intensities are much larger than those of the signal and idler, signal and idler photons are exchanged through coupled equations of motion possessing SU(2) symmetry, analogously to population transfer in coupled two-level quantum systems. **(c)**,**(d)** Analogy between Stark-chirped two-level atomic systems with field-free energies E_1, E_2 and four-wave mixing. $\hbar\Omega_P$ is the coupling pump's photon energy in two-level atomic systems. $\beta_i's$ (i = A,B,Sig,Idl) are wave-vectors of the four waves in FWM. Energy detuning Δ_0 corresponds to phase mismatch Δk, while Stark-induced energy shift Δ_S corresponds to Kerr-induced nonlinear phase modulation $\frac{\epsilon_0\chi^{(3)}\gamma_{int}}{2}(\omega_{\mathrm{B}}P_{\mathrm{B}} - \omega_{\mathrm{A}}P_{\mathrm{A}})$. The effective energy detuning Δ_{eff} is analogous to effective phase mismatch Δk_{eff}.

To mathematically demonstrate the concept, we start with simplified nonlinear Schrödinger equations under strong pump and plane, continuous wave (cw) approximations:

Optics EXPRESS

$$
\begin{aligned}
i\frac{dA_{\mathrm{A}}}{dz} &= \omega_A \epsilon_0 \chi^{(3)} \left(\frac{\mu_{A,A}}{2}|A_{\mathrm{A}}|^2 + \mu_{A,B}|A_{\mathrm{B}}|^2\right) A_{\mathrm{A}}, \\
i\frac{dA_{\mathrm{B}}}{dz} &= \omega_B \epsilon_0 \chi^{(3)} \left(\mu_{A,B}|A_{\mathrm{A}}|^2 + \frac{\mu_{B,B}}{2}|A_{\mathrm{B}}|^2\right) A_{\mathrm{B}},
\end{aligned} \tag{1}
$$

$$
\begin{aligned}
i\frac{dA_{\mathrm{Sig}}}{dz} &= \omega_{\mathrm{Sig}} \epsilon_0 \chi^{(3)} \left[\left(\mu_{\mathrm{Sig},A}|A_{\mathrm{A}}|^2 + \mu_{\mathrm{Sig},B}|A_{\mathrm{B}}|^2\right) A_{\mathrm{Sig}} + \gamma_{int} A_{\mathrm{A}}^{\dagger} A_{\mathrm{B}} A_{\mathrm{Idl}} e^{i\Delta k z}\right], \\
i\frac{dA_{\mathrm{Idl}}}{dz} &= \omega_{\mathrm{Idl}} \epsilon_0 \chi^{(3)} \left[\left(\mu_{\mathrm{Idl},A}|A_{\mathrm{A}}|^2 + \mu_{\mathrm{Idl},B}|A_{\mathrm{B}}|^2\right) A_{\mathrm{Idl}} + \gamma_{int} A_{\mathrm{A}} A_{\mathrm{B}}^{\dagger} A_{\mathrm{Sig}} e^{-i\Delta k z}\right].
\end{aligned} \tag{2}
$$

The waves are assumed to be linearly polarized and copolarized. The superscript † denotes a complex conjugate, A_i is the electric field envelope and $\mu_{i,j}$ (with i, j = A,B, Sig, Idl) and γ_{int} are nonlinear coupling coefficients for the two non-degenerate pumps (A,B), signal (Sig), and idler (Idl) waves [37]. The field envelopes are defined by $E_i = A_i e^{i(\omega t - \beta z)}$, where E_i are electric fields of the mixing waves normalized to their power P_i such that, $P_i = |E_i|^2 = |A_i|^2$, for i = A,B. For the sake of analytical simplicity, the transverse field distribution has been taken as wavelength-independent and ignored in this section under the plane wave approximation. $\Delta k = \beta_{\mathrm{A}} + \beta_{\mathrm{Sig}} - \beta_{\mathrm{B}} - \beta_{\mathrm{Idl}}$ is the wave-vector mismatch arising from dispersion of the propagation constants of the waveguided $\chi^{(3)}$ nonlinear medium. Under the undepleted pump approximation, the pump magnitudes are approximately constant, and their envelopes acquire only phase modulations due to self- and cross-phase modulation (SPM, XPM) during propagation, and thus their powers, P_i, remain constant. The phases of Pump A and Pump B are modulated by $\omega_{\mathrm{A}} \epsilon_0 \chi^{(3)} \left(\frac{\mu_{\mathrm{A,A}}}{2} P_{\mathrm{A}} + \mu_{\mathrm{A,B}} P_{\mathrm{B}}\right)$ and $\omega_{\mathrm{B}} \epsilon_0 \chi^{(3)} \left(\mu_{\mathrm{B,A}} P_{\mathrm{A}} + \frac{\mu_{\mathrm{B,B}}}{2} P_{\mathrm{B}}\right)$, accordingly. SPM and XPM between signal and idler waves are ignored due to their small amplitudes compared to the pumps. However, the signal and idler waves experience XPM from the pump waves, $\omega_{\mathrm{Sig}} \epsilon_0 \chi^{(3)} \left(\mu_{\mathrm{Sig,A}} P_{\mathrm{A}} + \mu_{\mathrm{Sig,B}} P_{\mathrm{B}}\right)$ and $\omega_{\mathrm{Idl}} \epsilon_0 \chi^{(3)} \left(\mu_{\mathrm{Idl,A}} P_{\mathrm{A}} + \mu_{\mathrm{Idl,B}} P_{\mathrm{B}}\right)$, as well as a mutual power transfer. By further approximating the nonlinear coupling coefficient to be wavelength-independent, i.e. $\mu_{i,j} = \gamma_{int}$, and introducing normalized amplitudes $C_{\mathrm{Sig}} = \frac{A_{\mathrm{Sig}} \exp\left(i\frac{1}{2}\left(-\Delta k + \epsilon_0 \chi^{(3)} \gamma_{int}\left(2\omega_{\mathrm{Sig}}(P_A + P_B) + \frac{1}{2}(\omega_A P_A - \omega_B P_B)\right)\right) z\right)}{\sqrt{\omega_{\mathrm{Sig}} \epsilon_0 \chi^{(3)} \gamma_{int} |A_A||A_B|}}$ and $C_{\mathrm{Idl}} = \frac{A_{\mathrm{Idl}} \exp\left(i\frac{1}{2}\left(\Delta k + \epsilon_0 \chi^{(3)} \gamma_{int}\left(2\omega_{\mathrm{Idl}}(P_A + P_B) - \frac{1}{2}(\omega_A P_A - \omega_B P_B)\right)\right) z\right)}{\sqrt{\omega_{\mathrm{Idl}} \epsilon_0 \chi^{(3)} \gamma_{int} |A_A||A_B|}}$, the coupled amplitude equations (CAEs) for the signal and idler waves (2) can be rearranged into the form:

$$
i\frac{dC_{\mathrm{Sig}}(z)}{dz} = \frac{\Delta k_{\mathrm{eff}}}{2} \cdot C_{\mathrm{Sig}}(z) + \frac{\kappa}{2} \cdot C_{\mathrm{Idl}}(z), \tag{3}
$$

$$
i\frac{dC_{\mathrm{Idl}}(z)}{dz} = \frac{\kappa}{2} \cdot C_{\mathrm{Sig}}(z) - \frac{\Delta k_{\mathrm{eff}}}{2} \cdot C_{\mathrm{Idl}}(z), \tag{4}
$$

where the effective wave-vector mismatch is $\Delta k_{\mathrm{eff}} = \Delta k + \frac{\epsilon_0 \chi^{(3)} \gamma_{int}}{2} (\omega_{\mathrm{B}} P_{\mathrm{B}} - \omega_{\mathrm{A}} P_{\mathrm{A}})$ and the coupling strength between the two waves is $\kappa = 2\epsilon_0 \chi^{(3)} \sqrt{\omega_{\mathrm{Sig}} \omega_{\mathrm{Idl}} \gamma_{int}^2 P_{\mathrm{A}} P_{\mathrm{B}}}$. This set of CAEs describing the wave mixing resembles the form of the SU(2) symmetric time-dependent Schrödinger equations of a coupled two-state atom except that time evolution in the quantum model has now become z propagation in the $\chi^{(3)}$ nonlinear medium. Whereas in an optically driven two-level atom, an effective energy detuning of the driving laser frequency from resonance, Δ_{eff}, is a sum of the detuning in the coupled two-level system, $\Delta_0 = E_2 - E_1 - \hbar\Omega_P$, and a field-induced Stark shift, Δ_s, the quantity analogous to the effective detuning for an exchange of the signal and idler wave amplitudes is an effective wave-vector mismatch, Δk_{eff}, which is a sum of the intrinsic wave-vector mismatch (i.e., when phase modulations are ignored), $\Delta k = \beta_{\mathrm{Sig}} + \beta_{\mathrm{A}} - \beta_{\mathrm{Idl}} - \beta_{\mathrm{B}}$, and XPM-induced phase modulations $\frac{\epsilon_0 \chi^{(3)} \gamma_{int}}{2} (\omega_{\mathrm{B}} P_{\mathrm{B}} - \omega_{\mathrm{A}} P_{\mathrm{A}})$ that

Optics EXPRESS

become important at high pump intensities. The coupling strength between the signal and idler states, κ, analogous to the interaction strength in two-level systems, depends on both the signal and idler's angular frequencies $\omega_{\mathrm{Sig}}, \omega_{\mathrm{Idl}}$, nonlinear coupling coefficient γ_{int} and the two pump intensities P_A, P_B. The analogous quantities are summarized in Table 1 and are depicted in Figs. 1(c)–1(d).

Table 1. **Analogy of FWM to a coupled 2-level atom**

Parameter	2-level atom	Four-wave mixing
Evolution parameters	time	z axis
Frequency detuning / Phase mismatch	Δ_0	Δk
Stark shift	Δ_S	$\frac{\epsilon_0 \chi^{(3)} \gamma_{int}}{2} (\omega_{\mathrm{B}} P_{\mathrm{B}} - \omega_{\mathrm{A}} P_{\mathrm{A}})$
Coupling coefficient	Ω_R	$\kappa = 2\epsilon_0 \chi^{(3)} \sqrt{\omega_{\mathrm{Sig}} \omega_{\mathrm{Idl}} \gamma_{int}^2 P_{\mathrm{A}} P_{\mathrm{B}}}$
Generalized "Rabi" frequency	Ω	$\sqrt{\kappa^2 + \Delta k_{\mathrm{eff}}^2}$

2.2. Adiabatic passage

Having identified a close analogy, the evolution dynamics of FWM under the undepleted pump approximation and with a photon exchange as drawn in Figs. 1(a)–1(b) can be expected to follow the known dynamics of SU(2) symmetric coupled two-level atomic systems. The simplest analogy is the case of constant Δk_{eff}, in which the difference between signal and idler photon numbers oscillates at the (spatial) Rabi frequency, $\Omega = \sqrt{\kappa^2 + \Delta k_{\mathrm{eff}}^2}$. As is the case in experimental atomic physics, Rabi flopping can be used to achieve a complete population inversion (in this case meaning all signal photons are converted to idler photons, or vice-versa, depending on which field has a nonzero initial ampitude), but only if the coupling lasts for exactly one-half of a Rabi oscillation ($z = \pi/\Omega$) and the detuning (Δk_{eff}) is zero. Thus, the final population is highly sensitive to the experimental parameters and is wavelength dependent. This solution is characterized by the well known efficiency-bandwidth trade-off: if the experiment is tuned perfectly for one signal-idler wavelength pair, i.e., $\Delta k_{\mathrm{eff}} = 0$ and the medium length $L = \pi/\Omega$, it will be improperly tuned for other signal-idler wavelength pairs, since Δk_{eff} is wavelength dependent. Broadband conversion is only achieved in the low conversion efficiency limit, i.e., when $L \ll \pi/\Omega$.

A second example is rapid adiabatic passage (RAP), which can be used to asymptotically achieve 100% population transfer from an initial state to a target state through a slowly swept energy detuning. Since the CAEs of our FWM model shares the same mathematical form as a two-level atomic system, RAP should also exist in FWM: if the effective wave-vector mismatch is swept from large positive value to large negative value (or vice-versa) adiabatically, the signal wave (initial state) shall fully convert to the idler wave (target state) without back-conversion. It can be shown that for our CAEs (3) and (4), the condition required for adiabatic following in AFWM is [38]:

$$|\dot{\kappa} \Delta k_{\mathrm{eff}} - \kappa \Delta \dot{k}_{\mathrm{eff}}| \ll \left(\kappa^2 + \Delta k_{\mathrm{eff}}^2\right)^{\frac{3}{2}}, \tag{5}$$

where the derivatives are with respect to propagation distance, z. Additionally, to ensure a robust adiabatic conversion, $|\Delta k_{\mathrm{eff}}| \gg \kappa$ is required at both the beginning and end of the photon exchange, i.e., the coupling between waves at the entrance and exit of the medium should be insignificant.

Nearly 100% photon conversion efficiency is expected to be achieved between signal and idler waves through AFWM if the adiabatic condition (5) is fulfilled, as has been demonstrated in $\chi^{(2)}$ nonlinear media using a swept wave-vector mismatch created by aperiodically poled

gratings [10, 11]. Moreover, a RAP-like frequency transfer can occur for each frequency within a broadband signal pulse in a single nonlinear medium [8, 9], and greater than octave-spanning bandwidths have been achieved through adiabatic three-wave mixing [11, 12]. The process is also expected to exhibit a linear transfer function of spectral phase and amplitude if the pump pulses have a relatively narrow bandwidth compared to the signal and idler pulses, as has also been demonstrated for RAP in three-wave mixing [12], offering a simple route towards arbitrary pulse shaping of the generated idler through pre-conversion amplitude and phase shaping of the signal.

We note that the distinguishing features of the driven two-level system analogy for FWM versus three-wave mixing include: first, that two nondegenerate pump waves are required to achieve SU(2) symmetric frequency conversion between signal and idler waves rather than one pump wave, and second, that the effective wave-vector mismatch Δk_{eff} is not only dependent on propagation constants β_i, but also on Kerr-induced nonlinear phase modulations $\frac{\epsilon_0 \chi^{(3)} \gamma_{int}}{2} (\omega_B P_B - \omega_A P_A)$. These features allow a wide range of possible implementations of RAP that are unique to the FWM system, including the possibility of a swept effective wave-vector mismatch derived from longitudinally increasing or decreasing phase modulations imparted by the two non-degenerate pumps (achieved through group-velocity walk-off, for example), an analogy of Stark-chirped rapid adiabatic passage [39]. In the case that a waveguided structure is used for the FWM interaction, RAP can be achieved through a longitudinal sweep of the waveguide dispersion, or by width modulation of the waveguide core. Two examples of waveguide-enabled AFWM are presented in Section 4.

3. Generalized propagation model

Here we develop a generalized analytical framework for rigorous numerical treatment of FWM processes that captures arbitrary time-dependent ultrashort pulses propagating in longitudinally-variant waveguides of a $\chi^{(3)}$ nonlinear medium. The analysis is suitable for arbitrary mode profiles and arbitrary waveguide geometries or material assuming the waveguide modes have negligible components in the direction of propagation. In Section 4, we apply the generalized framework to treat the AFWM frequency conversion scheme. Let us start with the nonlinear dynamical equations for propagation of an optical pulse in a waveguided system [37, 40],

$$\frac{dA(z,\omega)}{dz} = -i\omega \int\int \bar{P}_{NL}(x,y,\omega) \cdot \left(\vec{E_{0t}}^{\dagger} e^{i\beta(z,\omega)z}\right) dxdy, \tag{6}$$

where $\bar{P}_{NL}$ is the nonlinear polarization, the subscript $()_t$ stands for the transverse electric field, $()_{0t}$ refers to the transverse mode of the electric field profile of the waveguide, $\beta(z,\omega)$ is the propagation constant inside the waveguide, and $A(z,\omega)$ is the field amplitude spectral density for the transverse electric field, which is related to the electric field in time and space through an inverse Fourier transform: $\vec{E}_t(x,y,z,t) = \int_{-\infty}^{\infty} \frac{d\omega}{2\pi} \overbrace{\frac{1}{2}\left[A(z,\omega) + A^{\dagger}(z,-\omega)\right] \vec{E}_{0t}(x,y,z,\omega) e^{-i\beta(z,\omega)z}}^{\equiv \bar{E}_t(x,y,z,\omega)} e^{i\omega t}$.

In the case of centrosymmetric material, where the dependence of the nonlinearity on frequency is weak, the 3rd-order nonlinear coefficient tensor is $\chi^{(3)} = \chi^{(3)}_{xxxx} = \chi^{(3)}_{yyyy} = \frac{\chi^{(3)}_{\{yyxx\}}}{3}$, where the $\{\}$ stands for all permutations [41], and the nonlinear polarization takes the form $\bar{P}_{NL,k} = \epsilon_0 \chi^{(3)} \sum_{j \in x,y} \bar{E}_j(x,y,z,\omega) * \bar{E}_j(x,y,z,\omega) * \bar{E}_k(x,y,z,\omega)$, where $*$ stands for the convolution product. This yields the equation

$$\frac{dA(z,\omega)}{dz} = -i\omega\chi^{(3)} e^{i\beta(z,\omega)z} \iint \sum_{k \in x,y} \bar{P}_{NL,k} \cdot \left(\vec{E}_{0t,k}(x,y,z,\omega)^{\dagger}\right) dxdy. \tag{7}$$

Optics EXPRESS

In this article, we focus our investigation on FWM Scheme 1 from Fig. 1(a) with non-degenerate pump wavelengths. We wish to obtain a set of equations for describing the scheme, as in Eq.(1),(2), where the field amplitude spectral density now takes the form of an optical pulse. The spectral density is $A(z,\omega) = A_{\mathrm{A}}(z,\omega) + A_{\mathrm{B}}(z,\omega) + A_{\mathrm{Sig}}(z,\omega) + A_{\mathrm{Idl}}(z,\omega)$, where the $A_i(z,\omega)$ are the envelopes for field components centered around carrier frequency ω_i. We choose to ignore the polarization component corresponding to third-harmonic generation, due to the large phase mismatch of the process in our investigated platforms. We also ignore attenuation because of the short lengths of the platforms.

We first discuss implementations where non-overlapping spectral components among four waves can be approximated. By further approximating the transverse modes of the electric field profiles to those at their central wavelengths, Eq. (7) yields a set of four nonlinear coupled equations. For example, for the signal wave we obtain,

$$\begin{aligned}
&\frac{dA_{\mathrm{Sig}}(z,\omega)}{dz} = -i\omega\epsilon_0\chi^{(3)}e^{i\beta_{\mathrm{Sig}}(\omega)z}\times \\
&\Big[\gamma_{int}A_{\mathrm{B}}(\omega)\,e^{-i\beta_{\mathrm{B}}(\omega)z} * A_{\mathrm{Idl}}(\omega)\,e^{-i\beta_{\mathrm{Idl}}(\omega)z} * A_{\mathrm{A}}^{\dagger}(-\omega)\,e^{-i\beta_{\mathrm{A}}(\omega)z} + \\
&\frac{\mu_{\mathrm{Sig,Sig}}}{2}A_{\mathrm{Sig}}(\omega)\,e^{-i\beta_{\mathrm{Sig}}(\omega)z} * A_{\mathrm{Sig}}^{\dagger}(-\omega)\,e^{i\beta_{\mathrm{Sig}}(\omega)z} * A_{\mathrm{Sig}}(\omega)\,e^{-i\beta_{\mathrm{Sig}}(\omega)z} + \\
&\mu_{\mathrm{Sig,Idl}}A_{\mathrm{Idl}}(\omega)\,e^{-i\beta_{\mathrm{Idl}}(\omega)z} * A_{\mathrm{Idl}}^{\dagger}(-\omega)\,e^{i\beta_{\mathrm{Idl}}(\omega)z} * A_{\mathrm{Sig}}(\omega)\,e^{-i\beta_{\mathrm{Sig}}(\omega)z} + \\
&\mu_{\mathrm{Sig,A}}A_{\mathrm{A}}(\omega)\,e^{-i\beta_{\mathrm{A}}(\omega)z} * A_{\mathrm{A}}^{\dagger}(-\omega)\,e^{i\beta_{\mathrm{A}}(\omega)z} * A_{\mathrm{Sig}}(\omega)\,e^{-i\beta_{\mathrm{Sig}}(\omega)z} + \\
&\mu_{\mathrm{Sig,B}}A_{\mathrm{B}}(\omega)\,e^{-i\beta_{\mathrm{B}}(\omega)z} * A_{\mathrm{B}}^{\dagger}(-\omega)\,e^{i\beta_{\mathrm{B}}(\omega)z} * A_{\mathrm{Sig}}(\omega)\,e^{-i\beta_{\mathrm{Sig}}(\omega)z}\Big].
\end{aligned} \tag{8}$$

The z-dependence of A_i and β_i (i = A,B,Sig,Idl) was dropped from the notation for clarity (e.g., $A(\omega) = A(z,\omega)$), and we defined the following overlap integrals of the electric field transverse profiles: $\gamma_{int} = \frac{1}{2}\iint dxdy\Big[\left(\vec{E}_{\mathrm{B}}\cdot\vec{E}_{\mathrm{Idl}}\right)\left(\vec{E}_{\mathrm{A}}\cdot\vec{E}_{\mathrm{Sig}}\right) + \left(\vec{E}_{\mathrm{B}}\cdot\vec{E}_{\mathrm{A}}\right)\left(\vec{E}_{\mathrm{Idl}}\cdot\vec{E}_{\mathrm{Sig}}\right) + \left(\vec{E}_{\mathrm{Idl}}\cdot\vec{E}_{\mathrm{A}}\right)\left(\vec{E}_{\mathrm{B}}\cdot\vec{E}_{\mathrm{Sig}}\right)\Big]$ and $\mu_{i,j} = \frac{1}{2}\iint dxdy\left(|\vec{E}_i|^2|\vec{E}_j|^2 + 2|\vec{E}_i\cdot\vec{E}_j|^2\right)$. These overlap integrals are evaluated at the center wavelengths of each mixing wave. Due to the convolution product naturally appearing in these equations, it is more natural to introduce them in the time domain [42]. We define $B_i(z,\omega) = A_i(z,\omega)\,e^{-i\beta_i(z,\omega)z}$, and deduce a time-domain version of the four nonlinear coupled equations. For example, the equation for $B_{\mathrm{Sig}}(z,t)$ is,

$$\begin{aligned}
&i\frac{dB_{\mathrm{Sig}}(z,t)}{dz} = \\
&+\mathcal{F}^{-1}\Big[\beta_{\mathrm{Sig}}(z,\omega)B_{\mathrm{Sig}}(z,\omega)\Big] \leftarrow \text{Dispersion} \\
&+\varepsilon_0\chi^{(3)}\mathcal{F}^{-1}\Big[\omega\mathcal{F}\Big[\gamma_{int}B_{\mathrm{B}}(z,t)B_{\mathrm{Idl}}(z,t)B_{\mathrm{A}}{}^{\dagger}(z,t)\Big]\Big] \leftarrow \text{FWM} \\
&+\varepsilon_0\chi^{(3)}\mathcal{F}^{-1}\Big[\omega\mathcal{F}\Big[\sum_{\nu\in\mathrm{A,B,Idl}}\mu_{\mathrm{Sig},\nu}|B_\nu(z,t)|^2B_{\mathrm{Sig}}(z,t)\Big]\Big] \leftarrow \text{XPM} \\
&+\varepsilon_0\chi^{(3)}\mathcal{F}^{-1}\Big[\omega\mathcal{F}\Big[\frac{\mu_{\mathrm{Sig,\,Sig}}}{2}\left|B_{\mathrm{Sig}}(z,t)\right|^2B_{\mathrm{Sig}}(z,t)\Big]\Big] \leftarrow \text{SPM},
\end{aligned} \tag{9}$$

where $\mathcal{F}$ is the Fourier transform operator. The first term can be understood as the dispersion dynamics, second term is the exchange of energy between the four waves, and the third and fourth terms are the cross- and self-phase modulations, respectively. Cast in this way, the γ_{int} and $\mu_{i,j}$ overlap factors can be understood as the frequency dependent nonlinear coupling coefficients, which enables accurate evaluation of nonlinear frequency conversion strength in FWM. Eq. (9) mimics the traditional form of FWM processes by capturing phase-matched

3rd-order nonlinearities [37], i.e., those that are automatically phase matched (namely SPM and XPM), as well as non-degenerate FWM, which will be arranged to be phase matched in the applications of AFWM investigated below. However, Eq. (9) has improvements over the traditional form by capturing exact dispersion and self-steepening effect through the use of the Fourier transform operator rather than Taylor expansions. Under the above approximations, this is the general form of a FWM process depicted by Fig. 1(a), Scheme 1.

To consider implementations where the four waves do have overlapping spectral components, such as in the case of supercontinuum generation, or, as in our work, near-octave-spanning bandwidth generated by AFWM in optical fibers, we follow the same Fourier transform steps from Eq. (7) to Eq. (9), but maintain a single pulse simulation without splitting the spectral density or temporal envelope into four fields. To guarantee generality in optical fibers, we also include Stimulated Raman Scattering (SRS) and spontaneous emission. This results in a supercontinuum-like (1 + 1)-D generalized nonlinear Schrödinger equation (GNLSE):

$$\begin{aligned} &i\frac{dB(z,t)}{dz} = \mathcal{F}^{-1}\left(\beta(z,\omega)B(z,\omega)\right) + \varepsilon_0\chi^{(3)}\cdot \\ &\mathcal{F}^{-1}\left(\omega\cdot\gamma_{int}\cdot\mathcal{F}\left\{(1-f_R)\left|B(z,t)\right|^2\cdot B(z,t) + f_R B(z,t)\cdot\int_0^\infty h_R(t')|B(z,t-t')|^2dt'\right\}\right), \end{aligned} \tag{10}$$

where $B(z,t)$ is a single-field envelope with a frequency grid covering all four mixing waves. $B(0,t) = A_{\mathrm{A}}(0,t)e^{i(\omega_{\mathrm{A}}-\omega_0)t} + A_{\mathrm{B}}(0,t)e^{i(\omega_{\mathrm{B}}-\omega_0)t} + A_{\mathrm{Sig}}(0,t)e^{i(\omega_{\mathrm{Sig}}-\omega_0)t}$ is the sum of all input field envelopes, where ω_0 is the carrier frequency of the single-field envelope and here is chosen to be the center frequency of the frequency grid. A one-photon-per-mode noise seed with random phase is superimposed onto each spectral point in the frequency grid to simulate vacuum noise. The propagation constant $\beta(z,\omega)$ is numerically solved at each z-step for each frequency grid point, given the fiber geometry and material properties at the position. Thus, although Eq. (10) mimics the traditional form of GNLSE in treating supercontinuum generation [37], it has the advantage over the traditional form in that the chromatic dispersion term (first term on the right-hand side (RHS)) captures exact dispersion across the simulated frequency grid without making the Taylor series approximation. Moreover, due to the wide simulated spectral bandwidth, we use the frequency dependent nonlinear coefficient $\omega\cdot\gamma_{int}$ to account for the self-steepening effect. The dispersion of $\chi^{(3)}$ is ignored.

As opposed to the coupled-field model above, the single-field model captures all possible FWM terms involving two created photons and two annihilated photons through the second term on the RHS. This includes not only the desired FWM-BS of Scheme 1 $\left(\omega_{\mathrm{A}}+\omega_{\mathrm{Sig}} = \omega_{\mathrm{B}}+\omega_{\mathrm{Idl}}\right)$ and SPM/XPM $(\omega_i+\omega_j = \omega_i+\omega_j)$, but also, when combined with the vacuum noise seed, it captures unintended parametric FWM interactions, such as other FWM-BS processes, modulation instability and parametric amplification by degenerate and non-degenerate FWM, which can produce both new and overlapping Fourier components. Only third harmonic generation and other $3\rightarrow 1$ and $1\rightarrow 3$ photon interactions (Scheme 2) are excluded, which are expected to be minimal due to large wave-vector mismatch. However, in this model, the overlap factor γ_{int} must be treated as a constant across the frequency grid of the simulation to ensure conservation of photon number. Thus, while the model can capture all relevant parasitic processes, it cannot handle any differences in their relative strength that are due to the dispersion of the overlap factor. The last term on the RHS represents SRS, which is described by the convolution integral between the Raman response function $h_R(t)$ and the total intensity of the field. f_R represents the delayed Raman response's fractional contribution to nonlinear polarization.

In Section 4.1, Eq. (9) and the corresponding equations for the other three field components are numerically solved to capture the complex propagation dynamics of AFWM in a structured silicon photonics waveguide, where broad but non-overlapping pulse bandwidths and a highly modulated, longitudinally varying waveguide structure are employed. The inclusion of an overlap integral for

Optics EXPRESS

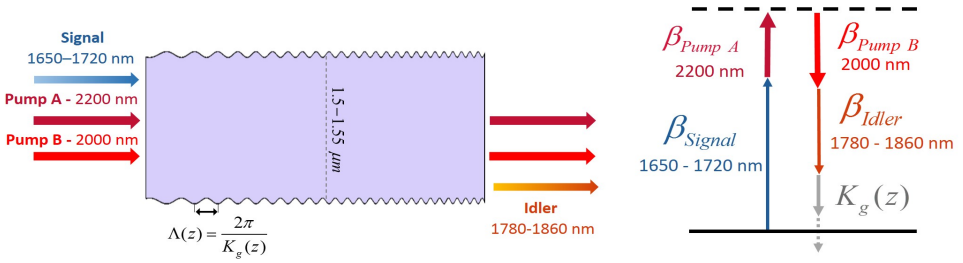

Fig. 2. Adiabatic frequency conversion in silicon photonics. (Left) The scheme allows an efficient broadband conversion of signal to idler waves (or vice-versa) by adiabatically changing the wave-vector mismatch through a chirped modulation of the width along the propagation direction. (Right) Momentum matching diagram (see Fig. 1(d)) illustrating the use of a variable effective momentum, $K_g(z)$, to longitudinally sweep the wave-vector mismatch. We have shown a near 100% conversion efficiency of an incoming signal spanning from 1.65-1.72 μm to an idler spanning from 1.78-1.86 μm.

each type of wave-mixing process allows accurate capture of their relative nonlinear coupling strengths. In Section 4.2, to capture AFWM in tapered optical fibers where the conversion bandwidth is nearly octave spanning, we find it is necessary to employ a single-field numerical framework using Eq. (10) to allow for capture of parasitic and unintended phase-matched FWM processes. Simulations for both platforms are described in the next section.

4. Potential platforms and simulations

In this section, we employ numerical investigations of broadband pulse propagation to illustrate how AFWM can be achieved in both silicon photonics structures and optical fibers, which are two platforms with broad interest to science and technology. For illustration of the AFWM concept, we choose to investigate broadband down-conversion as the application, and find conditions for efficient conversion in both platforms. We assume a fundamental mode evolution along the optical waveguides.

Eq. (5) suggests that AFWM can be achieved by longitudinal variation of either the effective wave-vector mismatch, Δk_{eff}, or the coupling strength, κ. Here, we explore straightforward control of the adiabatic condition through the waveguide geometry, which presents a controllable knob for tuning the propagation constants through waveguide dispersion and for tuning the overlap factors. Thus, in the following examples, we explore the use of longitudinal variations to the waveguide geometry to achieve the adiabatic condition of Eq. (5). Two distinct approaches are investigated. In the case of silicon waveguides, an aperiodic quasi-phase matching (QPM) approach is employed, utilizing cyclic modulations of the waveguide width to modulate the nonlinear coupling coefficients. This gives rise to a longitudinally varying effective momentum that can be used to offset the wave-vector mismatch. In the case of optical fibers, a linear variation of fiber core diameter is used to achieve a monotonic longitudinal sweep of Δk_{eff} through its effect on the waveguide dispersion.

4.1. AFWM in silicon photonics devices

Thanks to recent technological advances, control of the wave-vector mismatch parameter for realizing AFWM in silicon photonics might be achieved by several methods. One approach is to longitudinally sweep the width of the waveguide from one end to the other, thereby producing an adiabatic sweep of Δk_{eff} from a large positive value to a large negative one (or vice versa) through the contribution of the waveguide dispersion to the effective refractive index of the material. A second approach would be to apply a small periodic change in waveguide width

Optics EXPRESS

with a longitudinal chirp to the period (as illustrated in Fig. 2). This approach adds an effective momentum, $K_g(z) = 2\pi/\Lambda(z)$, to the effective wave-vector mismatch, Δk_{eff}, derived from the resulting modulation of the nonlinear coupling coefficient. Thus, the period of width modulations, $\Lambda(z)$, can serve as a highly tunable knob for controlling wave-vector mismatch. We define a wave-vector mismatch of the modulated process, $\Delta k_{\text{mod}}(z) = \Delta k_{\text{eff}}(z) + K_g(z)$. In this expression, we have explicitly included the longitudinal variation of Δk_{eff}, which is due to the cyclic variation in waveguide dispersion also arising from the modulation in width. As discussed below, the waveguided structure is designed to ensure that this variation has a negligible magnitude compared to the longitudinal sweep of Δk_{mod} imparted by $K_g(z)$.

Our numerical simulations are of Eq. (9) with no further approximations. However, in order to gain intuition regarding the physical mechanism prominent in the adiabatic width modulation scheme, the effective momentum from the QPM process can be derived in the following way. Assume the FWM has a periodically varying nonlinear coupling coefficient in the longitudinal direction: $\gamma_{int} = \gamma_{avg}\left[1 + s \cdot \cos\left(K_g(z) \cdot z\right)\right], s < 1$. This represents the nonlinear coupling coefficient of a silicon waveguide with width modulation period $\Lambda(z)$. γ_{avg} is the average nonlinear coupling coefficient, while s is half the maximum difference in coupling strength due to the width modulation. Rewriting the cosine in terms of two exponents, $2{\cdot}\cos\left(K_g(z) \cdot z\right) = \exp\left(iK_g(z) \cdot z\right) + \exp\left(-iK_g(z) \cdot z\right)$, will result in three terms, the unmodulated average term, and the two modulated terms contributing momenta $\pm K_g(z)$. The second term only further increases the wave-vector mismatch and thus plays an insignificant role for the intended FWM process. The first term, however, reduces the wave-vector mismatch for the intended process and offers a controllable wave-vector mismatch offset. The overall wave-vector mismatch of the modulated process reduces to $\Delta k_{\text{mod}}(z) = \Delta k_{\text{eff}}(z) + K_g(z)$, $K_g(z) = 2\pi/\Lambda(z)$, which enables the possibility of tuning the $\Delta k_{\text{mod}}(z)$ by scanning the effective momentum $K_g(z)$. This can be achieved by longitudinally chirping the waveguide width modulation period $\Lambda(z)$.

Our numerical simulations were based on the 4th-order Runge-Kutte method. Conversion efficiency was evaluated by the photon conversion ratio (PCR) parameter, defined as:

$$\text{PCR} = \frac{\text{idler final spectral density}}{\text{signal input spectral density}} \times \frac{\omega_{\text{Sig}}}{\omega_{\text{Idl}}}, \tag{11}$$

where ω_{Idl} and ω_{Sig} are the frequencies of each signal-idler pair. This definition is inherently normalized such that complete conversion of signal to idler without parasitic effects corresponds to a PCR of 1. We compare the performance of an adiabatic structure with chirped $\Lambda(z)$ to a standard QPM approach of using a constant-valued $\Lambda(z)$ chosen to phase match the carrier frequency. We find that the adiabatic structure results in a PCR that is larger than 0.9 for a broad range of frequencies, while the PCR of the standard QPM approach does not converge due to non-uniform conversion-back-conversion dynamics during propagation.

In the framework of a silicon waveguide compatible for an on-chip device, the minimum and maximum widths of the waveguide are set as restrictions. We simulated a Si rectangular waveguide with a tunable width restricted to the range 1.5-1.55 μm and with a constant height of 380 nm. Under these width restrictions, a monotonic sweep of the width of the waveguide would not yield the desired crossing of zero phase mismatch, and therefore the periodicity of a cyclic width variation is used as the knob for tuning the total modulated wave-vector mismatch, Δk_{mod}, along the waveguide. To realize efficient energy transfer, Δk_{mod} is varied longitudinally while fulfilling the condition presented in Eq. (5) (substituting Δk_{mod} for Δk_{eff}), by varying $1/\Lambda(z)$ from 2/mm to 20/mm. We choose to demonstrate this method by converting a signal ranging in wavelength from 1650-1720 nm to an idler of 1780-1860 nm. As another design consideration, in general one must be careful not to use a range of waveguide widths so large as to phase match unintended (parasitic) frequency conversion processes (as investigated in [43], for example). This can be avoided by setting the waveguide's length and modulation limits to be suitable for only the intended process. In the presented simulation of the silicon photonic waveguide, the

Optics EXPRESS

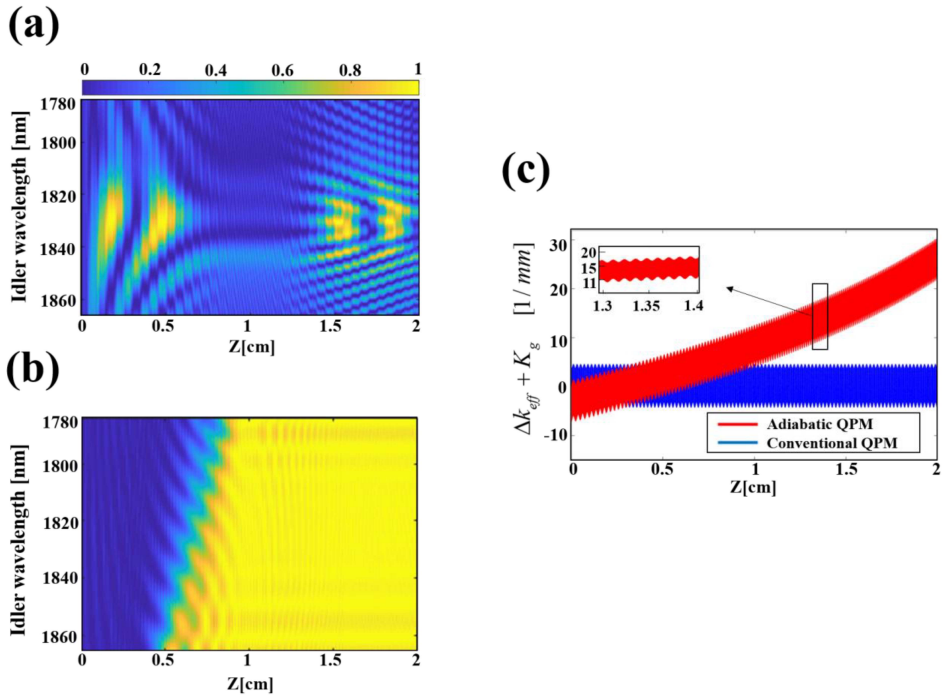

Fig. 3. Simulation results for an adiabatically modulated Si waveguide and for the standard periodic QPM approach. (a) Pseudocolor plot of idler intensity (arb. units) versus wavelength for the standard case of a periodic width modulation (i.e., constant-valued K_g) chosen to phase match only the central carrier wavelength. Efficiency is highly non-uniform and displays conversion-back-conversion cycles. (b) Pseudocolor plot of idler intensity (arb. units) versus wavelength for the adiabatic case, which shows nearly full and highly uniform conversion for all wavelengths included in the simulation. As expected, the locations where each wavelength has its rapid conversion jump are separated longitudinally. (c) The sum of effective phase mismatch and added momenta, $\Delta k_{\mathrm{mod}}(z)$, a multi-valued function corresponding to the wide range of signal (and corresponding idler) wavelengths. The overall shift is due to the longitudinal variation of $K_g(z)$, the effective momentum of the modulated waveguide, while the smaller oscillations are due to the modulation of the propagation constants due to the changing waveguide dispersion.

phase-matching conditions are restricted such that the modulated total phase mismatch of the desired scheme (i.e., $\omega_{\mathrm{Idl}} = \omega_{\mathrm{Sig}} + \omega_{\mathrm{A}} - \omega_{\mathrm{B}}$) crosses zero but is very large for the undesired scheme (i.e., $\omega_{\mathrm{Idl}} = \omega_{\mathrm{Sig}} - \omega_{\mathrm{A}} + \omega_{\mathrm{B}}$).

The FWM process is stimulated by the presence of two stronger narrow-band radiation sources centered at 2000 and 2200 nm. Our numerical simulations employed 1-ps Gaussian pump pulses with each having as little as 10-pJ energy, easily achieved from an oscillator. In this extremely low-energy scenario, the signal pulse energies, which are 60 fs at FWHM when compressed to be Fourier transform limited, can be as high as 0.5 pJ, with simulation results remaining the same (i.e., the conversion efficiency is > 90% for all wavelengths,). Our simulation results remain the same when pump and signal pulses are scaled together to much higher energies, for example with both pump pulses stretched to 5 ps with an energy of 10 nJ per pulse and with a signal pulse stretched to 500 fs with a pulse energy as high as 1 nJ. The simulated results presented in this section are for 1-ps, 10-pJ Gaussian pump pulses co-propagating with a 60-fs, 0.1-pJ

Optics EXPRESS

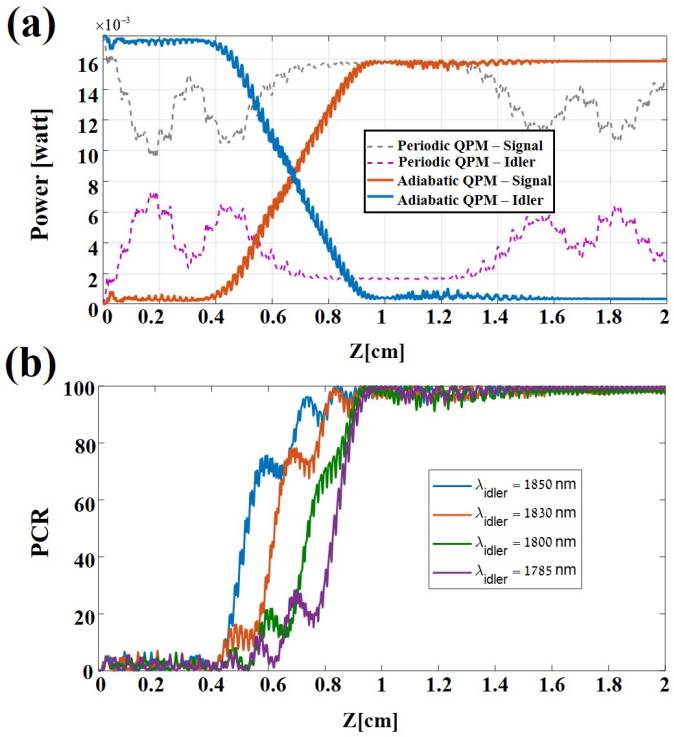

Fig. 4. (a) Integrated idler and signal powers during propagation in periodic and aperiodic (adiabatic) waveguides, illustrating signal-to-idler energy transfer. For the adiabatic evolution there is convergence of energy transfer from signal (blue) to idler (orange), while the conventional QPM case (gray, purple) shows unwanted back-conversion with efficiency that is non-uniform and highly sensitive to the initial conditions. (b) Efficiency vs. propagation length for various idler wavelengths in the adiabatic waveguide (corresponding to cross-sections of Fig. 3(a)). Illustrating evolution of an adiabatic nature, convergence is apparent for each wavelength, with rapid conversion taking place at a different location corresponding to the zero-crossing of the QPM wave-vector mismatch.

Gaussian Signal pump pulse. The group dispersion of our waveguide was analyzed according to the method of [44]. The dispersion obtained does not have a zero-dispersion wavelength (ZDW) between the fields and accurately matches previous reports [45], with group dispersion ranging from -1500 to -1000 [ps $\cdot$ km^{-1} $\cdot$ nm^{-1}].

For a waveguide with no modulation of width (results not shown), the wave-vector mismatch is always large and the conversion efficiency is poor (PCR < 0.04). For the waveguide with width modulated periodically to achieve QPM of the central idler wavelength (i.e., the conventional QPM approach), the efficiency is non-uniform and is highly sensitive to initial conditions, resulting in an output that is selective in wavelength [Fig. 3(a)]. In contrast, for the AFWM (adiabatic QPM) structure, all wavelengths gradually converge to a final state value close to full efficiency [Fig. 3(b)]. Induced oscillations in phase mismatch can been seen in the inset of Fig. 3(c). These oscillations, which are also present for the conventional QPM case, are the manifestation of the change in effective index due to modulation in that particular step. The width of the plotted modulated wave-vector mismatch is due to the broad bandwidth of the signal, since Δk_{eff} is wavelength dependent and takes a slightly different value for each wavelength. In addition, the QPM wave-vector mismatch is shifted from zero due to the XPM term in Δk_{eff}.

Optics EXPRESS

Figure. 4(a) illustrates the total conversion efficiency along the waveguide for a signal wavelength range spanning from 1650 to 1720 nm. As can be seen, pulses are converted with very high efficiency and converge to a final value, whereas the efficiency of the conventional QPM approach does not converge due to back-conversion. Furthermore, the intensities during propagation of the broadband signal and idler in the adiabatic frequency conversion scheme exhibit a robustness and superiority of power transfer when compared to the conventional QPM periodic scheme. Energy is shifted in an adiabatic manner and converges to a final state. In Fig. 4(b), the idler intensity is plotted for selected wavelengths in order to emphasize the convergence of the adiabatic solution to a final state for all wavelengths. It is worth noting that this type of structure can accommodate the conversion of a different idler range by an appropriate change to the designed width modulation periods, i.e., such that Δk_{mod} will contain a zero-crossing for each signal-idler pair while fulfilling Eq. (5).

4.2. AFWM in step-index fibers

In this section, we investigate the feasibility of AFWM frequency conversion in the simplest and most common fiber platform, step-index optical fibers (SIF). To achieve the longitudinal variation in Δk_{eff} needed for AFWM, we explore the use of a fiber taper to longitudinally sweep the waveguide dispersion contribution to the propagation constants. Our goal is to employ a long enough fiber with an adiabatic taper rate satisfying Eq. (5) to achieve efficient AFWM frequency conversion for an infrared bandwidth approaching a full octave.

As before, we focus our investigation on FWM Scheme 1 from Fig. 1(a). In the application modeled below, the second harmonic of $\mathrm{Pump_A}$ is used as $\mathrm{Pump_B}$. A signal with its wavelength between $\mathrm{Pump_A}$ and $\mathrm{Pump_B}$ is used to generate an idler wave with a longer wavelength than the three input waves. Given the wavelengths of typical modern pulsed lasers, this scheme would be convenient for near-IR and mid-IR generation. We investigate the cases where ω_{A} corresponds to 1.03, 1.55, or 2.0 μm. For applications in solid-core fibers involving four well-separated frequencies, the typical beam intensity (as limited by the laser damage threshold) is usually low enough to make the contribution to wave-vector mismatch from nonlinear phase modulations, $\frac{\epsilon_0 \chi^{(3)} \gamma_{int}}{2} (\omega_{\mathrm{B}} P_{\mathrm{B}} - \omega_{\mathrm{A}} P_{\mathrm{A}})$, much smaller than that from the propagation constants β_i (i.e., the intrinsic wave-vector mismatch). Therefore, we approximate $\Delta k_{\mathrm{eff}} \approx \beta_{\mathrm{A}} + \beta_{\mathrm{Sig}} - \beta_{\mathrm{B}} - \beta_{\mathrm{Idl}}$, and explore the conditions for which $\Delta k_{\mathrm{eff}} = 0$.

We consider a fiber with only one ZDW, as is the case for most commonly used SIFs. As is typically the case for FWM-BS processes, a symmetric placement of the four mixing frequencies around the ZDW enables phase matching [35,43]. As shown below, while phase matching can be achieved in other configurations, the broadest bandwidth is achievable in symmetric configuration, which is a successful approach even in the case of FWM frequencies separated by multiple octaves. Plots of propagation constant β against optical frequency ω are shown in Fig. 5 for $\mathrm{Pump_A}$ wavelengths corresponding to (a) Yb-doped, (b) Er-doped, and (c) Tm-doped fiber lasers, in either standard silica fiber, ZrF_4 fiber (Thorlabs P1-23Z models), and InF_3 fiber (Thorlabs P1-32F models), respectively. We define average propagation constants $\beta_{M_1} = \left(\beta_{\mathrm{A}} + \beta_{\mathrm{Sig}}\right)/2$ and $\beta_{M_2} = (\beta_{\mathrm{B}} + \beta_{\mathrm{Idl}})/2$. Achieving $\Delta k_{\mathrm{eff}} = 0$ thus requires $\beta_{M_1} = \beta_{M_2}$. If all four mixing waves are located on one side of the ZDW [Fig. 5(a)], the condition $\beta_{M_1} = \beta_{M_2}$ cannot be achieved, a consequence of the group-velocity dispersion $\beta'' = d^2\beta/d\omega^2 > 0$ for all frequencies. For typical single-mode fiber core radii (~2-8 μm), the ZDW (~ 1.27 μm) is longer than any wavelength of the four waves involved, and there is no phase matching for a wide idler range, as shown in Fig. 5(d). A similar conclusion can be drawn if all four waves lie within the $\beta'' < 0$ region. In contrast, if one wave is on the opposite side of the ZDW with respect to the other three waves [Fig. 5(b)], phase matching becomes possible, but only within a narrow range of parameters. As seen in Fig. 5(e), narrowband phase-matching conditions are achieved for only a small range of core radii.

Finally, if there are two waves on each side of the ZDW [Fig. 5(c)], the chance that $\beta_{M_1} = \beta_{M_2}$

Optics EXPRESS

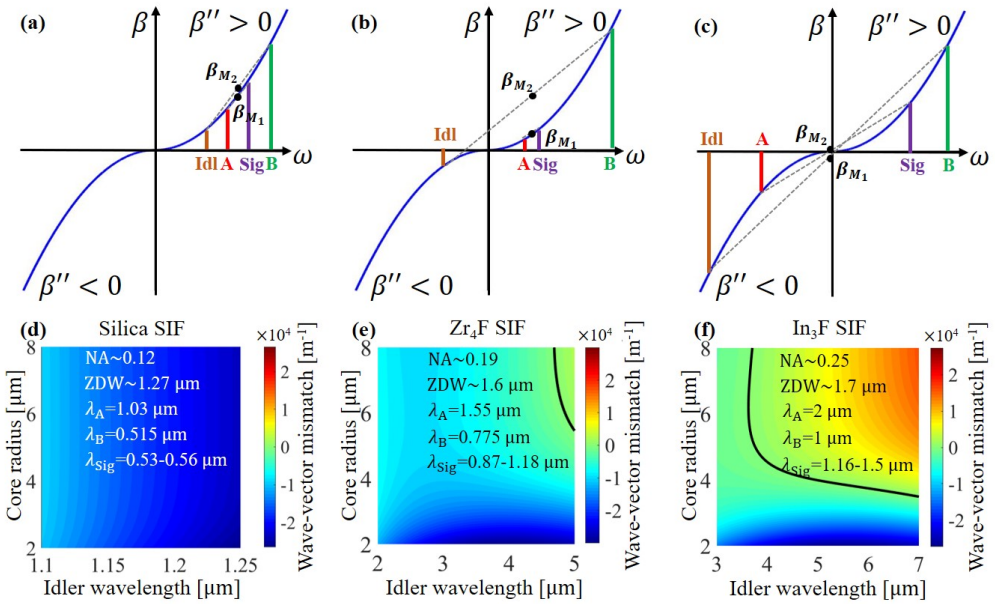

Fig. 5. The relative positions of the ZDW and optical wavelengths determine the likelihood of a broad phase-matching bandwidth for AFWM in SIF. Top row: Propagation constants of the four mixing waves where $\omega_A + \omega_{Sig} = \omega_B + \omega_{Idl}$ and $2\omega_A = \omega_B$, for three cases. The y-axis lies at the ZDW. Achieving $\Delta k_{eff} = 0$ requires $\beta_{M_1} = \beta_{M_2}$, where $\beta_{M_1} = (\beta_A + \beta_{Sig})/2$ and $\beta_{M_2} = (\beta_B + \beta_{Idl})/2$. Bottom row: wavevector mismatch versus fiber core radius and idler wavelength for laser parameters corresponding to each case. **(a),(d)** Case for a standard silica SIF where all four waves are on one side of the ZDW. No phase matching is possible. **(b),(e)** Case where one frequency is on the opposite side of the ZDW from the other three. Narrowband phase matching under limited conditions is possible. The black curve represents contour zero ($\Delta k_{eff} = 0$). **(c),(f)** Case where there are two waves on each side of the ZDW. Phase matching is probable in this case, and gives rise to conditions where an octave-spanning idler wave covering 3.5-7 μm can be phase matched in an AFWM process in a tapered fiber.

becomes much higher. As seen in Fig. 5(f), an octave-spanning range of idler wavelengths can be phase matched over a core radius range spanning 3.5-7 μm. In an untapered fiber, Δk_{eff} will equal zero for only one idler frequency, and the conversion bandwidth will be limited to the standard phase-matching bandwidth. In contrast, a tapered fiber with an adiabatic taper rate according to Eq. (5) over this range of core radii could be used to achieve AFWM over the full octave-spanning wavelength range, offering a route to dramatically increase the conversion bandwidth. We conclude that a ZDW lying between pairs of interacting wavelengths maximizes the possibility for a broad AFWM conversion bandwidth in a tapered SIF.

To examine AFWM in tapered SIF with ultrashort pulses, we numerically solved the (1 + 1)-D GNLSE representing Scheme 1 $\left(\omega_A + \omega_{Sig} = \omega_B + \omega_{Idl}\right)$, Eq. (10), as discussed in Section 3. The frequency grid used in the simulation covers a multi-octave bandwidth spanning from 450 nm to 9 μm. Analytical eigenvalue equations for SIF are used to determine the longitudinally varying propagation constant $\beta(z, \omega)$ [37]. We found SRS to be negligible due to the short length of the fiber simulated and the low Raman gain for fluoride fibers with picosecond transform-limited (TL) pump durations [46]. Therefore, SRS terms in Eq. (10) were ignored. The GNLSE numerical simulation captures both intended and unintended FWM processes, giving guidance for choosing parameters that deliver optimal AFWM without exciting significant parasitic effects

Optics EXPRESS

upon generation of the desired idler wave.

Motivated by its wide potential AFWM frequency conversion bandwidth, we investigated fiber parameters corresponding to Figs. 5(c) and 5(f). The transparency range of Thorlabs P1-32F fibers is listed as 310 nm to 5.5 μm (for attenuation < 3 dB/m). Therefore, we expect a lower than 0.25 dB attenuation (> 95% transmission) in this spectral range if a short (~cm) fiber is used. We chose intensity, chirp rate, and fiber length to optimize the generation of mid-IR light by AFWM while maintaining an insignificant amount of parasitic effects. The simulated fiber has a core radius taper from 4.5 μm to 3.55 μm over a length of 5 cm, resulting in a phase-matching range for idler wavelengths covering 4-7 μm, although we only expect high transmission for wavelengths up to 5.5 μm. According to our calculation, a peak power of >180 kW for each of the two pumps would fulfill the adiabatic condition, Eq. (5), across this entire bandwidth. We note, while we employed a linear taper rate in this study, a nonlinear taper could be employed as well. In either case, a rule for achieving high conversion efficiency is adherence to Eq. (5) for every frequency in the pulse, where Eq. (5) is satisfied for each frequency independently and is evaluated locally in the fiber where its wave-vector mismatch crosses zero.

The input pulse characteristics were chosen to be realizable using common fiber laser technology. The pumps were chosen as a 10-ps full-width at half maximum (FWHM) TL Gaussian pulse at 2.0-μm wavelength and its second harmonic, a 7.1-ps FWHM TL Gaussian pulse at 1.0 μm, each having peak power of 110 kW (which is slightly lower than the ideal power and was chosen to avoid strong parasitic FWM found at higher peak powers). We chose to employ picosecond pump pulse durations because of three reasons. 1) The group-velocity walk-off between the pump and signal pulses through the simulated fiber is ~ 1 ps. 2) Pumps with picosecond TL durations excite fewer parasitic nonlinear effects compared to femtosecond pulses, due to their narrower bandwidth. We note that the pump bandwidth is broadened due to SPM/XPM during the interaction, and care must be taken to keep it appropriately narrow (i.e., to avoid parasitic effects that can be identified through the simulation) during the interaction. 3) Given the peak power needed to fulfill the adiabatic condition, the fiber damage threshold prevents the use of pulse durations $\gg$ 10 ps. The signal pulse was a chirped 2-ps FWHM Gaussian pulse spanning 1360-1440 nm, with a peak power of 10 kW. The corresponding idler range spans 4250-5140 nm. We simulated the nonlinear propagation of the three waves through the optical fiber, each in their respective fundamental mode. At each longitudinal fiber position, the nonlinear coupling coefficient (overlap factor) γ_{int} in Eq. (10) was evaluated from the overlap integral calculated based on the effective areas determined by finite element method at the center frequencies of the four waves of the intended AFWM. The obtained value was used for a constant γ_{int} over the entire simulated frequency grid at the corresponding longitudinal position, while its value changes as a function of tapered fiber core diameter as the waves propagate through the full fiber length.

Figure. 6 shows numerical solution of the (1+1)-D GNLSE for the parameters discussed above. Figure. 6(a) shows the power spectral density evolution of the 4-5.5 μm mid-IR region as the three input pulses propagate through the 5-cm-long tapered fiber. The generated idler wave inherits the Gaussian spectral profile of the signal wave. PCR evolution for selected wavelengths is shown in Fig. 6(b). Each mid-IR wavelength is produced with evolution dynamics typical of RAP, and with longitudinally varying conversion position, as expected due to the variation in core size where the $\Delta k_{\text{eff}} = 0$ condition is encountered for different wavelengths. The PCR at the fiber exit is shown in Fig. 6(c) for the full idler bandwidth, spanning 4.2-5.2 μm, and is above 0.7 for the full range. The generated mid-IR pulse is centered at 4.7 μm and has an output energy of 5.5 nJ, with chirped ~2 ps FWHM duration and ~3 kW peak power. If fully compressed to its ~43 fs TL duration, the sub-3-cycle mid-IR pulse can reach a peak power of 94 kW, thus indicating a new route to high peak power, fiber-based few-cycle pulse sources.

To further investigate the adiabatic character of the conversion and the influence of parasitic

Optics EXPRESS

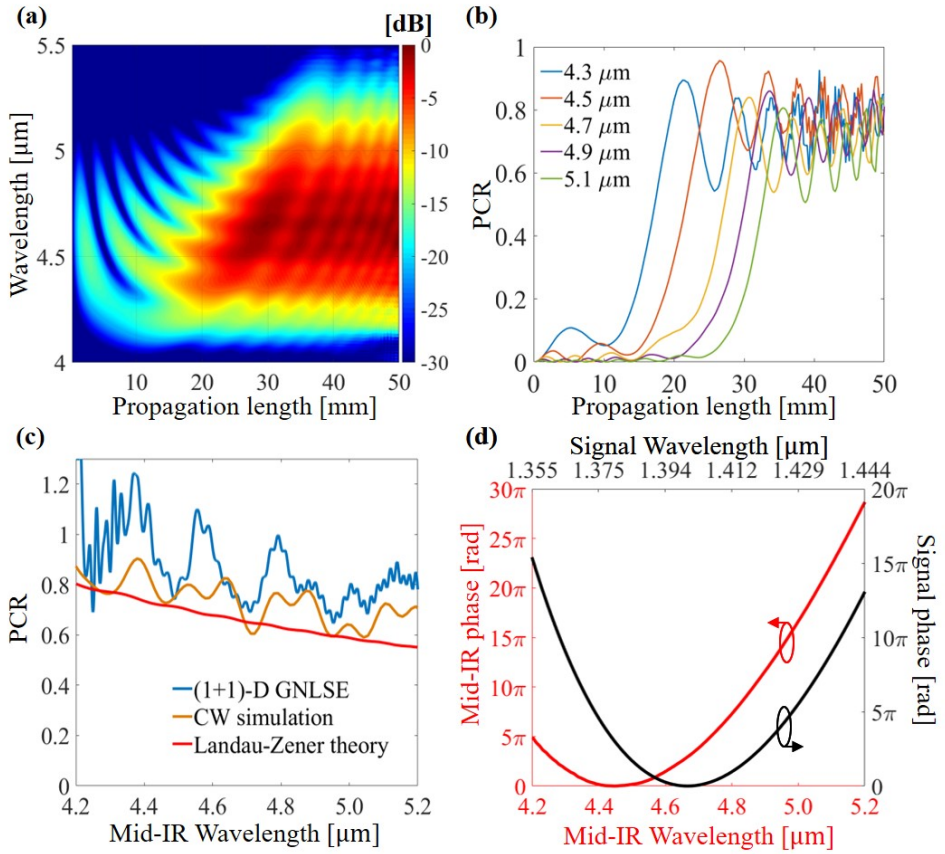

Fig. 6. Mid-IR generation via AFWM in InF_3 SIF with core radius tapered from 4.5 to 3.55 μm over a 5-cm length. **(a)** Mid-IR beam spectral density evolution along the propagation axis, given a Gaussian input signal spectrum. AFWM can be observed for 4.2-5.2 μm. **(b)** Evolution of PCR for selected wavelengths. **(c)** PCR at the fiber exit vs. idler wavelength. Due to parasitic FWM amplification of the input signal, PCR determined by solution of the GNLSE is higher than that predicted by the cw simulation and includes values greater than 1. **(d)** Comparison between the spectral phases of the output mid-IR and input signal waves indicates the coherence of the generated wave. The idler's phase consists of a conversion phase due to the wavelength-dependent conversion position (which is largely an effective third-order dispersion) plus the initial linear chirp (parabolic phase) of the signal pulse.

FWM, Fig. 6(c) includes for comparison both an analytical calculation of the expected conversion efficiency based on Landau-Zener theory of adiabatic transition probability [47,48], and numerical integration of the GNLSE for each signal-idler pair under the approximation that they are cw and that the AFWM interaction of Scheme 1 is the only FWM interaction. The cw simulation thus excludes pulse propagation, parasitic FWM, and SPM/XPM. It can be observed from Fig. 6(c) that the PCR expected from Landau-Zener theory matches the cw simulation well. Oscillations in PCR in the cw simulation result from non-apodized coupling (low-amplitude conversion-backconversion cycles) between signal and idler waves still existing at the fiber exit, as observed in Fig. 6(b). The PCR obtained from the full GNLSE simulation also matches the cw result well, but with slightly higher efficiency attributed to the parasitic process $\omega_A + \omega_B = \omega_{Sig} + \omega^*$, where ω^* is an unintended generated optical frequency. This parasitic process amplifies the input

signal by the strong pumps as if an optical parametric amplifier, resulting in a slightly amplified signal wave before its conversion to mid-IR takes place by AFWM. This process produces a PCR even greater than 1 for some wavelengths, a feature that potentially could be exploited in an application. However, fast oscillations in PCR appear at the short wavelength edge in Fig. 6(c) as a result of interference between the generated AFWM idler and parasitic cascaded FWM processes. We note that the relative weight of parasitic effects may be slightly higher than this model predicts, since the overlap factor for the intended AFWM process is slightly lower than that for FWM processes involving only visible and near-IR wavelengths.

Finally, the spectral phases of the input signal and output idler waves are presented in Fig. 6(d), showing coherent idler generation through AFWM. The quadratic phase of the chirped input signal is transferred to the mid-IR idler. An effective third-order dispersion can be observed, which is due to the longitudinally varying wavelength-dependent conversion position.

5. Summary and outlook

In this article, we introduced the concept of adiabatic four-wave mixing frequency conversion, a concept that should enable tunable, broadband, efficient, robust, and energetic frequency conversion in cubic nonlinear media for a broad range of applications. Theory and formula describing the analogy of RAP in SU(2)-symmetric FWM schemes were presented, culminating in the presentation of an adiabatic condition for FWM frequency conversion. Illustrating the wide applicability of the concept, two very different waveguided optical platforms were explored, using numerical modeling that captures the effects of broadband pulse propagation with longitudinally changing waveguide dimensions and a wide range of phase-matched nonlinear processes.

In silicon photonics devices, AFWM frequency conversion could be used for on-chip devices for applications such as conversion between lossless and dispersionless bands, sensing, computational manipulations and encryptions. A possible realization for an on-chip waveguide was suggested and simulated, with standard height for a silicon platform as well as standard sized widths, allowing a structure that could be incorporated easily as an on-chip device. We demonstrated a solution that suggests an efficient, robust, and broadband frequency conversion, with a bandwidth of up to 70 nm centered at 1820 nm, which is the first solution to our knowledge for such wide spectral widths. We have demonstrated this via simulation for an incoming broadband signal centered at 1680 nm and an outgoing idler of the same bandwidth centered at 1820 nm, with a PCR over 0.9. Similar structures could be easily designed to fit any desired signal-idler wavelength pairs desired on-chip without changing the overall size and geometry of the device.

In a step-index fiber platform, AFWM can be realized by using a tapered fiber. It was shown that a ZDW positioned in the middle of the four wavelengths is optimal for broadband phase matching of AFWM frequency conversion. A tapered InF_3 fiber was numerically simulated with a (1+1)-D nonlinear Schrödinger equation model. A broad 4.2-5.2 μm mid-IR bandwidth with flat PCR close to 1 was demonstrated. The proposed AFWM experimental parameters can be realized potentially in an all-fiber based system pumped by a Er-doped master oscillator. Pulse generation at the 2-μm pump wavelength with similar pulse duration and peak power has been reported, using a multi-stage thulium-doped fiber amplifier chain [49]. Pulses with bandwidth and center wavelength corresponding to the signal (1360-1440 nm, 2-ps chirped pulses) have been demonstrated using soliton self-frequency shift and dispersive wave generation using a 1550-nm Er-doped fiber source and highly nonlinear fiber [50]. The entire pulsed laser system might consist of an Er-doped fiber master oscillator front end used to pump soliton self-frequency shift as well as supercontinuum generation in highly nonlinear fiber to generate a 2-μm component that can be used to seed a multi-stage thulium-doped fiber amplifier. The high-energy 1-μm pump can be obtained by second harmonic generation of the 2-μm pump, or, alternatively, by using the supercontinuum to seed a multi-stage Ytterbium-doped fiber amplifier. The source and AFWM stage could therefore be an all-fiber based system.

Optics EXPRESS

While the simulated SIF platform can be tuned for the phase matching of other frequencies by an adjustment of the material type and dimensions of the tapered fiber, other fiber platforms may offer advantages for a specific spectral range and for other power levels. For example, our initial calculations predict hollow core fibers, including hollow core PCFs and microstructured fibers, to be potential platforms for AFWM. These fibers can handle orders-of-magnitude higher intensity than SIF due to their gaseous core, and typically have a much wider transmission window than solid core fibers [51]. Furthermore, the dispersion of hollow core fibers can be flexibly controlled by fiber geometry design, and thus may offer a flexible approach to the design of a waveguide that fits the needs of a particular application. The introduction of gases into holey fibers can also be used to tune their nonlinearity and dispersion, and pressure gradients might be used as another means for controlling the longitudinal variation of parameters used to fulfill the adiabatic condition. Therefore, we expect HCFs to provide an important platform for high power and high energy frequency conversion through AFWM processes.

We note that the FWM-BS scheme simulated in the examples of Section 4 is widely used for applications ranging from tunable wavelength conversion in the telecom band to quantum frequency conversion [35, 52–54], and recent work has reported broadband frequency conversion with a preserved pulse shape [43]. In recent years, FWM-BS has become an actively studied scheme for low-noise preparation and translation of single-photon states [36, 55–57]. In each of the above contexts, use of the adiabatic counterpart of the FWM-BS scheme may bring significant value by broadening the effective conversion band while also providing robust and high conversion efficiency and a linear phase transfer.

More generally, the ubiquitous presence of cubic nonlinearity potentially opens the AFWM concept to any waveguided optical platform that can handle the typical field strengths needed for FWM. While not all media can be expected to offer an opportunity for broadband conversion in a single device, not all relevant applications would require it. One might envision, for example, a frequency domain wavelength multiplexing scheme with a device tailored for each channel. In such an application, the robust and efficient qualities of adiabatic conversion – back-conversion free and signal intensity independent conversion with near-100% efficiency – could be beneficial. The expanded bandwidth of AFWM compared to conventional FWM can be expected to have a strong impact in many areas, such as up-conversion detection for sensing, spectroscopy, and imaging, or for the efficient generation of a hyperspectral range of wavelengths in an ultrafast laser system, potentially covering frequencies from UV to far-IR. Moreover, the linearized transfer function of amplitude and phase of a 1-to-1 photon up-conversion or down-conversion scheme such as this when pump pulse bandwidths are significantly narrower than those of the signal and idler – already demonstrated for octave-spanning conversion in adiabatic three-wave mixing processes [12] – may be used to greatly simplify dispersion management, expand the effective bandwidth of pulse shapers, or be utilized to preserve information in sensing, communications, or encryption applications.

Funding

United States-Israel Binational Science Foundation (BSF) (2014360); Israel Science Foundation (ISF) (1433/15); PAZY foundation (PAZY-YS16-9002); Air Force Office of Scientific Research (FA9550-13-1-0159).

Acknowledgments

X. D. and J. M. thank Logan Wright, Noah Flemens and Walter Fu for helpful discussions.